eChem
https://www.sciltp.com/journals/eChem

Article

Pulsed Thermal Shock Enables Deep Heteroatom Substitution and Substantial Reduction of Graphene

Kai Wang [1,*], Tao Jia [1], Xu Zhang [1], Yufang Ren [1], Fengxiao Hou [1,*], Yuexian Song [1], Xiaobin Zhong [1], Yangang Zhang [1], Yaohui Zhang [1], Junfei Liang [1,*] and Hua Wang [2,*]

[1] Key Laboratory of Shanxi Province for Solar Thermal Technology, School of Energy and Power Engineering, North University of China, Taiyuan 030051, China
[2] Key Laboratory of Bio-Inspired Smart Interfacial Science and Technology of Ministry of Education, School of Chemistry, Beihang University, Beijing 100191, China
* Correspondence: wangkai92@nuc.edu.cn (K.W.); mercatushou@outlook.com (F.H.); junfeiliang@buaa.edu.cn (J.L.); wanghua8651@buaa.edu.cn (H.W.)

How To Cite: Wang, K.; Jia, T.; Zhang, X.; et al. Pulsed Thermal Shock Enables Deep Heteroatom Substitution and Substantial Reduction of Graphene. *eChem* **2026**, *2*(1), 3. https://doi.org/10.53941/echem.2026.100003

Received: 26 March 2026
Revised: 24 May 2026
Accepted: 3 June 2026
Published: 18 June 2026

Abstract: Developing efficient synthesis routes for heteroatom-doped graphene materials is of great significance for advancing high-performance energy storage systems. Herein, a rapid and scalable strategy for constructing B-substituted reduced graphene oxide (RGO-B) via pulsed rapid joule heating (PRJH) was demonstrated, enabling deep bulk-phase B incorporation and efficient thermal reduction with O removal. Zeta potential and Kelvin probe force microscopy (KPFM) analyses reveal that B substitution effectively modulates the electronic structure of graphene, resulting in a less negative surface and an increased work function, thereby significantly enhancing its rate capability. Remarkably, deeply heteroatom B-substituted graphene induces surface folding and interlayer spacing expansion, effectively increasing accessible active sites available for Li^+ storage. Electrochemical tests demonstrate that the RGO-B electrode delivers a specific capacity of 415.5 mAh/g after 800 cycles at 0.5C, and maintains a capacity of 115.9 mAh/g after 20,000 cycles at an ultrahigh rate of 13C with a capacity retention exceeding 100%, exhibiting exceptional long-term cycling stability. These results highlight the great potential of RGO-B for ultra-long-cycle energy storage applications.

Keywords: pulsed rapid joule heating; heteroatom B; electronic structure; interlayer spacing; electrochemical performance

1. Introduction

Graphene, a two-dimensional material consisting of a single layer of carbon (C) atoms arranged in a sp^2-bonded honeycomb lattice, is regarded as a revolutionary material in both scientific and industrial communities due to its exceptional electrical and thermal conductivity, mechanical strength, and optical properties [1–6]. Engineering the crystal structure and atomic composition of graphene enables precise property control. In this regard, heteroatom doping (e.g., N, B, S, F, P) constitutes one of the most facile and versatile strategies, owing to its simplicity and efficacy in modulating the material's physical and chemical properties [7–12]. Heteroatom functionalization of graphene is primarily achieved through two routes: in-situ doping and post-treatment. The in-situ doping route simultaneously accomplishes graphene synthesis and heteroatom incorporation, with chemical vapor deposition and solvothermal methods being representative strategies [13,14]. However, these in-situ doping routes are often time-consuming (hours or days), with solvothermal methods further accompanied by high solvent consumption. In contrast, post-treatment methods utilize pre-formed graphene or graphene oxide as precursors, as exemplified by techniques such as thermal annealing, ball milling, plasma-induced, and laser heating [15–18]. However, a fundamental challenge in these post-treatment routes is the preferential dopant incorporation at edges

or defects, which disrupts the intrinsic sp^2-hybridized C network, introduces impurities, and can severely compromise the structural integrity when strongly oxidizing precursors are employed.

Flash Joule heating (FJH) has emerged as an ultra-fast synthesis technique that utilizes electrical current to rapidly elevate material temperature to 10^2–10^5 K within millisecond-to-second timescales, thereby activating targeted chemical reactions. This method employs the raw materials themselves as heating media, enabling highly efficient and direct energy conversion without solvents or catalysts [19,20]. Since 2020, FJH has proven to be an effective strategy for graphene production, converting solid carbon precursors into flash graphene through the synergistic effects of high temperature and electric field [21]. Currently, this technique is being extended as a platform for the rapid synthesis of various heteroatom-substituted flash graphene materials [22–27]. However, the scale-up of FJH technology faces significant challenges in terms of equipment capacity and the safety of associated capacitor systems [28]. In parallel, the direct current-powered rapid Joule heating (RJH) technique shares the ultra-fast kinetics characteristic of FJH (Figure S1, Supporting Information). This technique has been widely applied in carbon fiber graphitization, high-entropy alloy synthesis, rapid ceramic sintering, and graphene doping [29–32].

In this work, we establish a pulsed rapid joule heating (PRJH) technique without catalysts or solvents that enables simultaneous thermal reduction of graphene oxide (GO) and efficient deep substitution of heteroatom B into the C framework through synergistic modulation of thermal and electric fields. The process converts GO to RGO at 2700 °C (4 cycles × 10 s) while doping RGO/B to RGO-B at 1350 °C (10 cycles × 3 s) in a single operational platform. Firstly, this work commenced with density functional theory (DFT) simulations to evaluate the binding energies and electronic structure evolution during Li^+ migration for various B–C/B–C–O, B–O and B-B configurations. These theoretical insights directly informed the optimization of PRJH parameters for precisely synthesizing high performance RGO-B functional materials. Subsequently, coupled characterization via zeta potential, Kelvin probe force microscopy (KPFM), and high-resolution transmission electron microscopy (HRTEM) revealed how deep heteroatom B substitution modulates the surface electronic structure and bulk interlayer spacing. Ultimately, the resulting RGO-B electrodes demonstrate exceptional rate capability under 20,000 cycles at an ultrahigh 13C rate, which is attributed to the accelerated transport of both Li^+ ions and electrons induced by deeply B heteroatom-substituted graphene.

2. Materials and Methods

2.1. Synthesis of RGO-B

The commercial micron-sized graphene oxide (GO) sheets (purchased from Qingdao Yanhai Carbon Materials Co., Ltd., Qingdao, China.) have a thickness of several hundred nanometers, which used as precursors for dynamic pulsed rapid joule heating. 2.0 g GO particles were precisely loaded into a quartz tube and uniaxially compressed into a cylindrical pellet. The packing density was carefully modulated to achieve a bulk resistivity of 1.2 Ω (below the 6.0 Ω threshold). All joule heating treatments were carried out under a controlled argon atmosphere with vacuum conditions maintained at approximately −0.09 MPa. The sample first underwent three preliminary joule annealing cycles at 15 A and 20 V to stabilize its structure, followed by four pulsed rapid joule heating cycles at 50 A and 30 V, during which the temperature rapidly reached approximately 2700 °C. The final product, collected as thermally reduced graphene oxide (RGO), was obtained with high structural integrity and electrical conductivity. Subsequently, 0.1 g of B and 1.9 g of RGO were dispersed in 100 mL of deionized water and magnetically stirred for 180 min to form a homogeneous mixture. The resulting suspension was freeze-dried to obtain the RGO/B precursor. The precursor was then subjected to ten consecutive dynamic pulsed rapid joule heating cycles at 45 A and 20 V, reaching a peak temperature of approximately 1350 °C under argon atmosphere with mild vacuum conditions. This process resulted in the formation of a B-deep-doped RGO matrix, which was designated as RGO-B.

2.2. Electrode Material Preparation

The prepared GO, RGO, RGO-B samples were individually blended with carbon black (conductive agent) and polyvinylidene fluoride (binder) in N-Methyl-2-pyrrolidone at a mass ratio of 8:1:1, respectively. The resulting slurry was uniformly coated onto a copper foil current collector and dried at 80 °C for 12 h in a vacuum oven. The obtained areal mass loading of electrodes with a diameter 14 mm was about 2.78 $mg \cdot cm^{-2}$. The polyethylene membrane (Cellgard 3200) was used as the separator, and the electrolyte consisted of 1.0 M LiPF6 dissolved in a mixture of ethylene carbonate, diethyl carbonate and ethyl methyl carbonate (1:1:1 in volume ratio) solvent with 5% fluoroethylene carbonate as an additive. All CR2032 coin cells were assembled in an argon-filled glove box with water and oxygen levels maintained below 0.01 ppm.

2.3. Materials Characterization

The morphology and elemental distribution of the samples were characterized using a field emission scanning electron microscope (FESEM, Zeiss Supra-55), high-resolution transmission electron microscopy (HRTEM, JEM-2100F) and energy dispersive spectroscopy (EDX Oxford Inca). The phase composition was characterized by X-ray diffraction (XRD, Shimanzu XRD-6000). The atomic concentration and valence status changes were tested using X-ray photoelectric spectrometer (XPS, ESCALAB250). The specific surface area and pore structure of the samples were characterized using a physical adsorption analyzer with N_2 as the adsorbent (BET, AUTOSORB-IQ-MP). The electrical conductivity of the as-synthesized samples was measured using a four-point probe powder resistivity measurement system (ST2722-SZ). Surface zeta potential measurements were performed in deionized water at 25 °C using a Zetasizer Nano instrument (NANOTRAC WAVE II). Atomic Force Microscope (AFM, Dimension Icon) was employed to characterize sample topography, including thickness, wrinkle distribution, and surface roughness. The probes used featured a typical tip radius of R = 25 nm, with cantilever dimensions of L = 225 μm in length, 2.8 μm in thickness, and W = 35 μm in width, and a spring constant of k = 3 N/m. Kelvin probe force microscopy (KPFM, SCM-PIT-V2) was employed to map the surface potential distribution of various samples in a non-invasive manner, revealing local work function variations at the nanoscale. Secondary ion mass Spectrometry (SIMS, ON-TOF.SIMS5) was used to characterize the two-dimensional (2D) and three-dimensional (3D) distribution of individual elements of B, C and O in RGO-B sample at varying depths. The cycle and rate performance of the assembled cells were tested using the BTS7.6.0 battery system with the voltage window of 0.01–2.50 V.

2.4. Simulation Model Methods

The Vienna Ab Initio Package (VASP) code was employed to perform all the DFT calculations with periodic boundary condition, including energy calculation, geometry optimization and electronic structure characteristics [33–35]. The GGA-PBE function in the projected augmented wave (PAW) method was used to describe the electron exchange correlation interaction, and the D3(BJ) method was used for dispersion correction to illustrate the weak interaction. The cut-off energy used for the calculation is 500 eV, the convergence accuracy of the electron step is 10^{-5} eV, and the convergence accuracy of the ion step is 0.02 eV/Å. A 4 × 4 × 1 Monkhorst-Pack k-point grid for Brillouin zone integration [36,37]. The vacuum layer of 15 Å was used avoid the influence of z-direction periodicity. Moreover, the Binding energies ($E_{binding}$) are calculated as $E_{binding} = E_{Total} - E_{surface} - E_{Li}$, where $E_{binding}$ is the binding energy, eV; E_{Total} is the total energy of the bound configuration, eV; $E_{surface}$ is the energy of pristine electrode materials, eV; E_{Li} is the energy of isolated Li^+ ions, eV. Finally, the transition state of the Li diffusion process was calculated by the climbing image–nudged elastic band (CI-NEB) method. The energy barriers of the process were calculated by the difference of the transition state energy and initial geometry energy, and the relative energy of final state was also calculated based on the initial state energy.

3. Results and Discussion

The circuit diagram of the pulsed rapid joule heating (PRJH) setup is shown in Figures 1a and S2, Supporting Information. The DC power supply (3000 W, 36 V × 83 A) enables an ultra-rapid Joule heating process with achievable temperatures ranging from 400 to 3600 °C. The entire synthesis process is exceptionally rapid. The pulsed Joule thermal reduction of GO to RGO achieved 2700 °C in just 40 s (4 cycles × 10 s duration), while the heteroatom B doping from RGO/B to RGO-B reached 1350 °C in only 30 s (10 cycles × 3 s duration), as shown in Table S1, Figures S3 and S4, Supporting Information. Meanwhile, the RGO and RGO-B samples achieved high mass yields of 96 and 99%, respectively (Table S2), with negligible mass loss, demonstrating the energy-efficient and environmentally friendly advantages of the PRJH technique.

Joule heating has been widely recognized as a highly effective technique for infusing heteroatom B into C matrix [7,11,28]. However, the success of substitution critically depends on achieving deep and uniform distribution of heteroatom B within the C matrix, along with the formation of specific chemical bonds, which are fundamentally linked to the overall enhancement of electrochemical performance. Thus, based on the preceding analysis, we constructed four atomic configurations: RGO, RGO-B1 (B atom substitution forming B-C/B-C-O bonds), RGO-B2 (B atom substitution forming B-O bonds) and RGO-B3 (B atom substitution forming B-B bonds) in order to simulate the potential bonding types during the PRJH process (Figure S5, Supporting Information). The binding energies and electronic structure characteristics of the configurations during Li^+ ions migration were evaluated using density functional theory (DFT) simulations. The binding energies of the RGO-Li, RGO-B1-Li, RGO-B2-Li and RGO-B3-Li configurations are −3.0834, −3.9221, −3.3609 and −3.6702 eV, respectively. The results demonstrate that the RGO-B1-Li configuration has the largest absolute value of binding energy, indicating

its highest structural stability during Li^+ migration (Figure 1b; Table S3, Supporting Information). The corresponding energy barriers for Li^+ migration under different structural configurations are 1.1743, 0.0751, 0.2407 and 0.1125 eV, respectively, which reveal that the RGO-B1-Li configuration exhibits the lowest energy barrier, indicating that a smaller barrier facilitates easier Li^+ ion migration. Namely, the formation of B-C/B-C-O bonds enhances the stability of Li^+ ion migration (Figure 1c; Table S4, Figure S6 and S7, Supporting Information).

The spatial distribution of the electron density difference during Li^+ ion migration (Figure 1d, Table S5, Supporting Information) further reveals that the RGO-B1-Li configuration exhibits the largest isosurface, indicating the most significant electron transfer. Quantitative analysis shows that the O ion in the RGO-B1 gains 0.33 charge, which is higher than those in the RGO-B2 and RGO-B3 configurations. Although the O ion in the RGO configuration gains a higher charge of 0.35 charge, this charge is primarily derived from the significant electron loss (0.4 charge) of the adjacent C atom. In contrast, the C atom bonded to the O loses only 0.08 charge in the RGO-B1 configuration. Collectively, electronic structure analysis indicates that the RGO-B1 configuration is more stable. In summary, the simulation results demonstrate that the B-C/B-C-O bonds formed in the RGO structure after the PRJH process are most conducive to the migration of Li^+ ions and electrons.

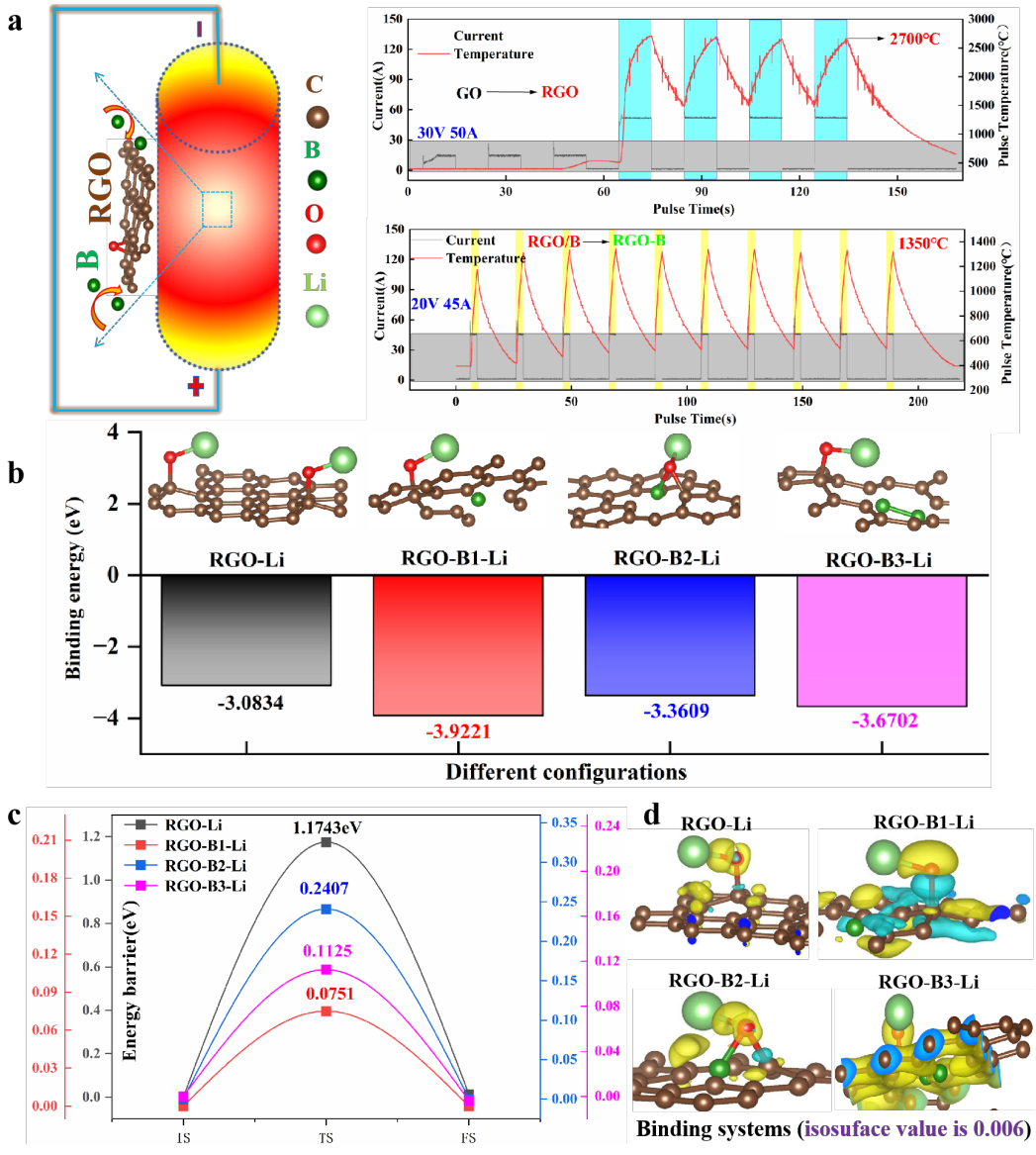

Figure 1. (**a**) Process flowchart for the synthesis of RGO and RGO-B by PRJH method; (**b**) Binding energy and (**c**) Energy barrier for Li migration under different configurations; (**d**) Electron density difference distribution during Li migration process.

The X-ray diffraction (XRD) patterns (Figure 2a) show consistent peaks at 26.4°, 42.4°, 44.5°, 54.5°, and 77.4° for all samples, corresponding to the (002), (100), (101), (004), and (110) planes, respectively, confirming the preservation of the C crystal structure after different PRJH treatments. The RGO-B composite exhibits a broad

low-intensity peak at approximately 9°, which is tentatively attributed to a phase formed by the bonding of B with C or O [15,38]. The X-ray photoelectric spectrometer (XPS) analysis (Figure 2b) indicates that the two-step PRJT process induces an effective thermal reduction of GO, as evidenced by a sharp decrease in O concentration (from 22.2 to 2.2%) and a concurrent increase in C content (from 77.8 to 95.8%), accompanied by the incorporation of B (2.0%). The C 1s spectrum (Figure 2c) shows a significant 20.57% contribution from C-B bonds. Meanwhile, the B 1s spectrum is dominated by B-C-O/B-C configurations (79.5%), alongside B-O (3.4%) and B-B (17.1%) bonds [7,39,40]. Quantitative analysis further reveals that the B-C-O/B-C ensemble is dominated by B-C (37.8%), BCO_2 (31.8%), and BC_2O (9.9%) configurations, which prior DFT simulations have demonstrated to be conducive to rapid ion and electron migration, thereby enhances the charge transfer capability of the material. The BET specific surface areas of GO, RGO, and RGO-B are 23.24, 21.53, and 18.25 m^2/g, respectively. Figure 2d,e further reveal that the PRJH treatment not only modifies the chemical bonding but also tailors the pore architecture, with the average pore size of RGO-B increasing from 13.6 to 21.2 nm. Furthermore, all samples exhibit a common trend of decreasing resistivity with increasing pressure (Figure 2f), with RGO-B achieving the lowest average value (from 0.011 to 0.006 Ω·m). The results collectively demonstrate that B doping via PRJH method is highly effective in enhancing the overall conductivity.

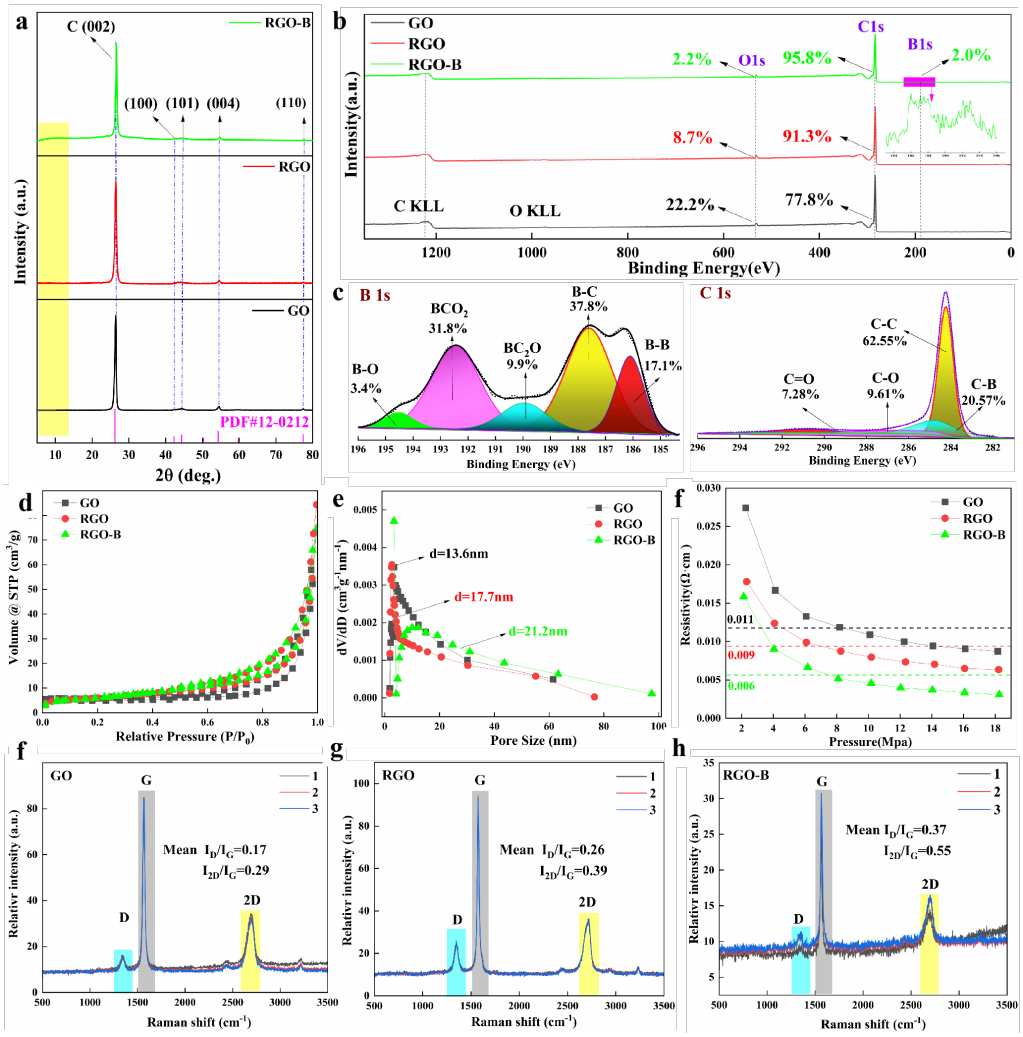

Figure 2. (**a**) XRD pattern; (**b**) XPS spectrum; (**c**) B 1s and C 1s XPS spectra; (**d**) Adsorption isotherm; (**e**) Pore size distribution; (**f**) Resistivity as a function of pressure; (**f–h**) Raman spectra for GO, RGO, and RGO-B.

Representative averaged Raman spectra of GO, RGO, and RGO-B are shown in Figures 2f–h and S8, each derived from three sampling points. All spectra exhibit three characteristic bands: the D band at ~1358 cm^{-1}, corresponding to the breathing mode of sp^2-C atoms in six-membered rings and correlating with the defect density; the G band at ~1574 cm^{-1}, arising from the in-plane bond stretching of sp^2-C pairs; and the 2D band at ~2712 cm^{-1}, originating from second-order zone-boundary phonons and positively scaling with graphene crystallinity. Raman analysis reveals that the I_D/I_G ratios of GO, RGO, and RGO-B are all substantially below 1, with mean values of 0.17, 0.26, and 0.37, respectively, which significantly lower than those reported in literature for doped graphene

systems [11,19,28]. This indicates that although the defect-related D-band intensity of RGO-B increases after the PRJH process, its overall defect density remains low, thereby preserving the long-range ordered lattice structure of graphene. This experimental finding is consistent with the preceding DFT calculations, which predict a weakened interplay between defects and dopants. Notably, the progressive increase in I_{2D}/I_G ratio from 0.29 to 0.55 further confirms that the PRJH technique simultaneously enables lattice repair of GO and substitutional B-doping, effectively tuning the electronic band structure while preserving long-range order.

The microstructure and morphology of all samples were characterized using field emission scanning electron microscope (FESEM), transmission electron microscopy (TEM), energy dispersive spectroscopy (EDX), and secondary ion mass spectrometry (SIMS) techniques, with the results shown in Figure 3. Compared to GO, both RGO and RGO-B processed by the PRJH technique display pronounced curved folds (Figure 3a, Figures S9–S11, Supporting Information). The curved folds appear as the residual gases remaining through the weak interfaces of GO during the thermal reduction and heteroatom doping process [17,33]. Figure 3b displays the HAADF image at different regions of the RGO-B sample. Both region ① and local region ③ show relatively uniform distributions of elements B, C, and O (Figure S12, Supporting Information), whereas local region ② corresponds to a B–O enriched area on the sample surface. HRTEM analysis of the RGO-B sample (Figure 3c) further confirms the formation of stable B–C bonds, evidenced by a lattice plane spacing of d = 0.213 nm. Deep heteroatom B doping increases the (002) lattice plane spacing from 0.335 nm in RGO to 0.342 nm in RGO-B (Figure S13, Supporting Information). The enlarged lattice plane spacing reduces the energy barrier for Li^+ ion transport, enhancing the kinetic performance of the electrode material [11,17].

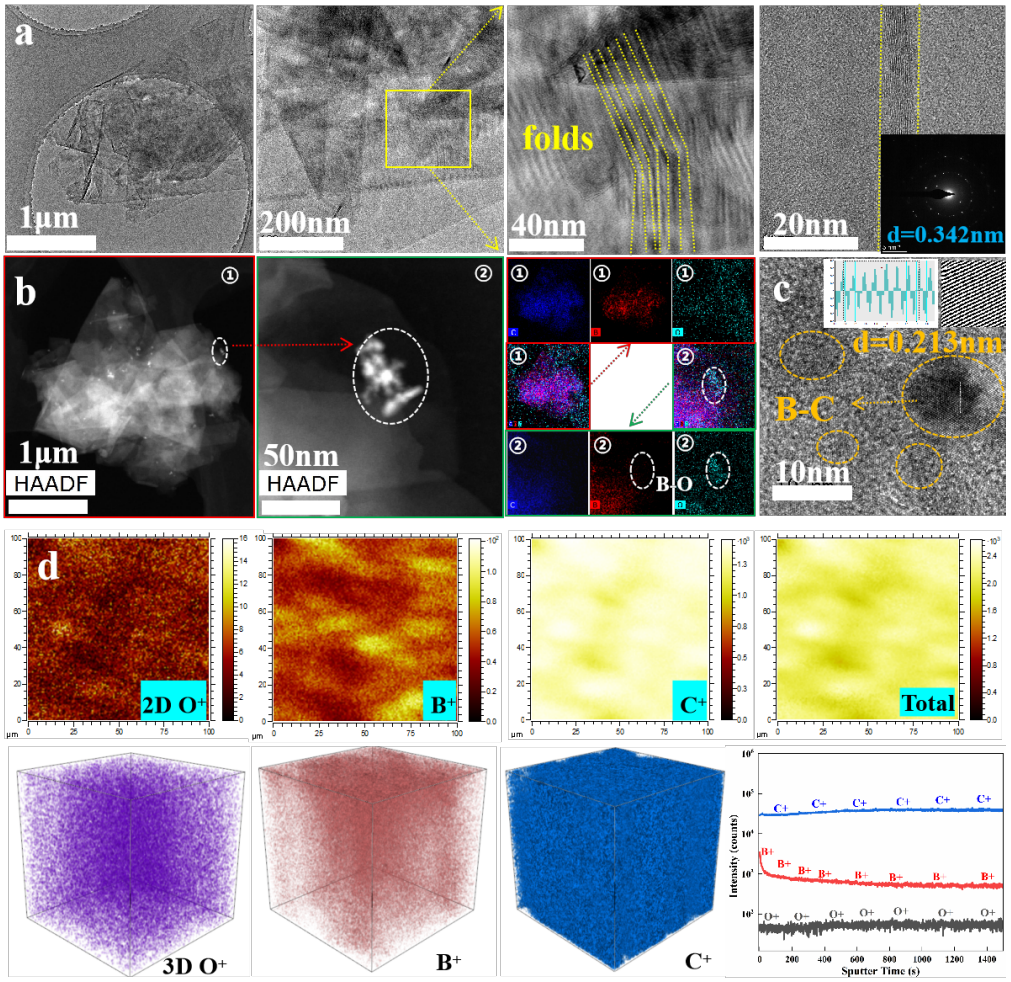

Figure 3. (**a**) TEM images at different magnifications, (**b**) EDX elemental mapping, (**c**) HRTEM image and (**d**) 2D and 3D SIMS analysis of RGO-B after 10 cycles PRJH.

The SIMS analysis of RGO-B after 10 cycles PRJH process in Figure 3d shows that the spatial distributions of the matrix elements C and minor O are relatively homogeneous, whereas the doped element B exhibits significant diffusion behavior during the initial sputtering stage, with its concentration gradually decreasing until reaching a uniform distribution in the final sputtering zone. The influence of pulse thermal shock on B diffusion

kinetics was systematically examined by 2D and 3D color total SIMS maps and different element distributions of RGO-B samples processed with 3 cycles versus 10 cycles PRJH (Figure S14, Supporting Information). It was observed that the B distribution after 3 and 10 cycles PRJH treatment both exhibit diffusion and stable zones. The RGO-B sample after 10 cycles PRJH shows a more homogeneous B distribution overall, with the B concentration in its stable zone being approximately half an order of magnitude higher than that in the 3 cycles PRJH sample. Compared to 3 cycles PRJH treatment, the 10 cycles PRJH reduces the O concentration by approximately threefold while achieving a more homogeneous distribution (Figure S15, Supporting Information). The schematic illustration of elemental migration (Figure S16, Supporting Information) elucidates a dual mechanism where pulsed thermal shock simultaneously drives O removal via thermal reduction and enables uniform and deep incorporation of B heteroatoms into the C crystal structure through bulk-phase diffusion.

Atomic force microscope (AFM) was employed to characterize the layer morphology evolution (Figure 4a–d). It was found that the samples of RGO and RGO-B processed by PRJH method display pronounced curved folds and a reduced thickness. The thicknesses of GO, RGO, and RGO-B are 609.3, 230.3, and 110.3 nm, respectively (Figure S17, Supporting Information), suggesting that the pulsed rapid thermal field not only induces stacking thickness but also promotes structural folding. Analysis indicates that the O-containing functional groups between GO layers rapidly decompose during the instantaneous ultra-high temperature of the PRJH process, generating gases such as CO_2 and H_2O vapor. The gases instantaneously create high local pressure, which acts like micro-explosions that pry apart the stacked layers, thereby achieving physical exfoliation and reducing the stacking thickness [5,11,28]. Furthermore, numerous thermal-induced bubbles formed on the surface of the RGO-B, which resulted from the pulsed rapid cycles under the pulsed heating and cooling fields. This process further promotes the stabilization of the incorporated B heteroatom in the form of B-O/B-C-O bonds within the C based material.

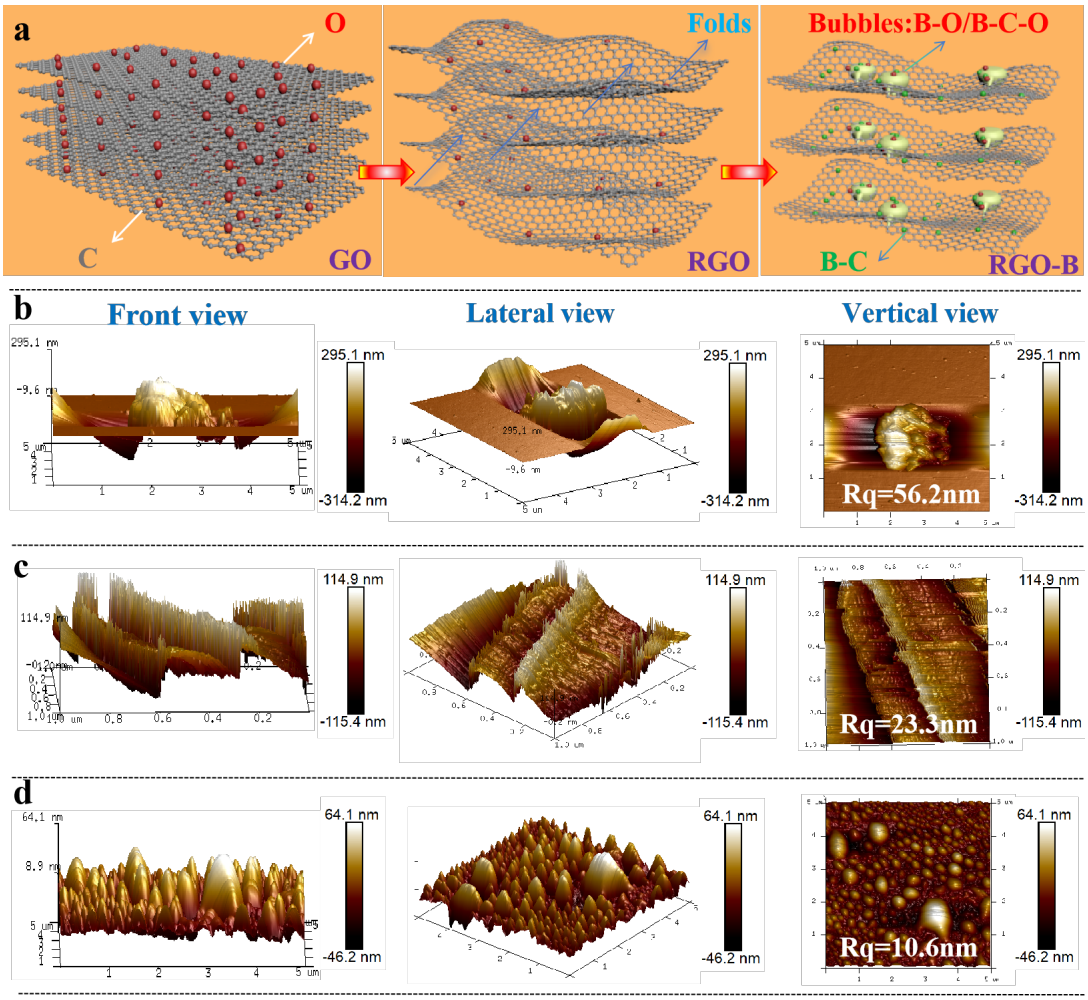

Figure 4. (**a**) Schematic illustration of layer morphology evolution during the PRJH process; AFM height distribution images at different views for (**b**) GO, (**c**) RGO, (**d**) RGO-B.

Three-dimensional kelvin probe force microscopy (KPFM) imaging was utilized to map the surface potential distribution, revealing nanoscale work function variations (Figure 5). The increase in work function can suppress

the decomposition of the electrolyte, reduce the formation of by-products, and thereby effectively control the cycling stability of the solid electrolyte interphase (SEI) [34,35,41]. The surface potential of GO, RGO, and RGO-B span 691.4 mV–1.0 V, 798.3 mV–1.0 V, and 965.6 mV–1.1 V, respectively. The results show that RGO-B exhibits a higher surface potential than both RGO and GO, indicating an increase in work function. This provides direct evidence that the B-doped pulsed thermal reduction effectively lowers the Fermi level of the C matrix, confirming the role of B as an electron-acceptor in modulating the electronic structure. Surface potential line-scan profiles further reveal spatial variations in work function across localized regions. The results indicate that the crest regions of RGO folds (points D and F) exhibit surface potentials of 0.98 V and 0.96 V, respectively, significantly higher than the value of 0.86 V measured in flat areas (point E). This result demonstrates that the folding morphology generated during the induced reduction of GO to RGO via PRJH process effectively enhances the work function. The bubble region (point H) exhibits the maximum surface potential of 1.07 V, indicating the highest work function at B-C/B-C-O enriched sites.

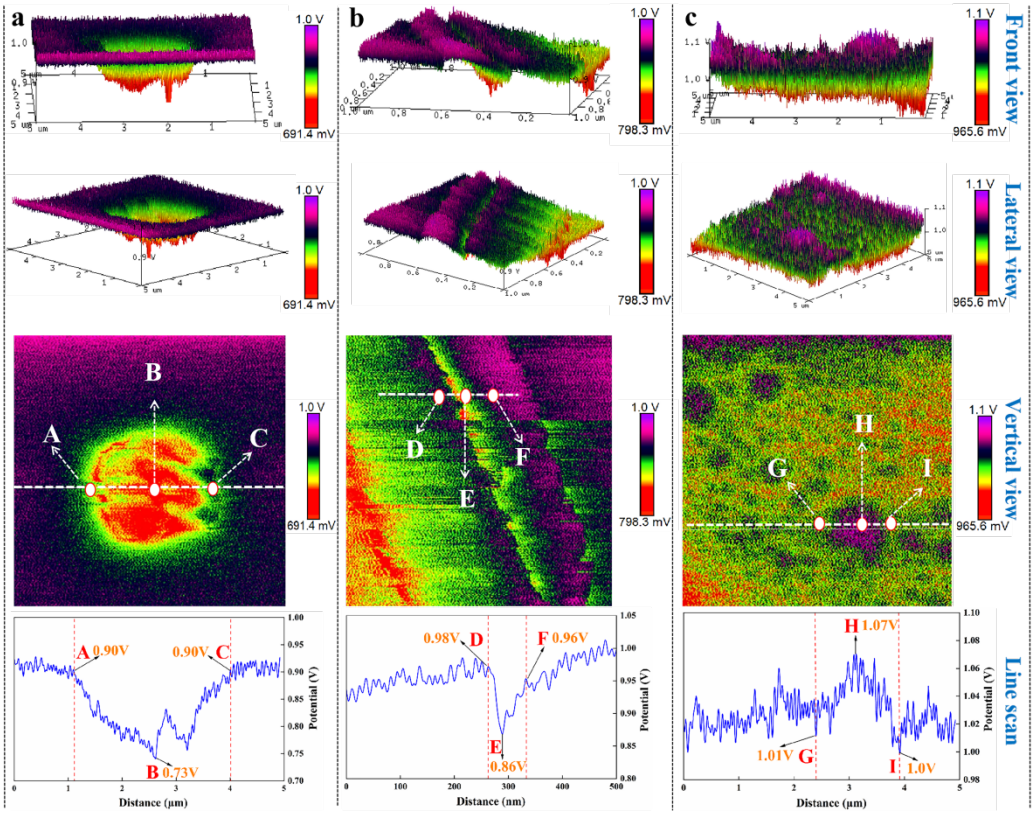

Figure 5. Three-dimensional front, lateral, and vertical views of KPFM surface potential mapping with corresponding local line-scan profiles for different samples: (**a**) GO, (**b**) RGO, (**c**) RGO-B.

Zeta potential measurements were further employed to elucidate the evolution of the material's surface chemical properties (Figure S18, Supporting Information) [38]. The measured zeta potentials of GO, RGO, and RGO-B are −81.2, −65.4, and −43.7 mV, respectively. The results show that RGO-B exhibits the smallest magnitude of negative zeta potential, indicating the lowest net negative charge density on its surface. This reduction in surface charge magnitude confirms the electron-accepting role of B in the C lattice. The reduced surface negativity of RGO-B suggests a lower energy barrier for Li^+ ions migration, thereby improving cycling stability and rate capability, which is proved by the previous DFT calculations of the RGO-B1-Li model. Thus, coupled analysis of zeta potential and KPFM confirms that deep heteroatom B doping effectively modulates the electronic structure, creating a surface with weaker negativity and higher work function. This not only verifies successful substitution of heteroatom B but also directly correlates with its superior electrochemical performance, such as long cycling life at ultrahigh rate.

The rate performance of LIBs reveals that the initial discharge specific capacities of GO, RGO, and RGO-B electrodes at current densities of 0.2, 0.5, 1.0, 2.0, 3.0, 5.0, and reset to 0.2 A/g reach 458.1/448.5/697.9, 331.8/355.1/402.3, 224.7/303.0/385.5, 60.1/136.6/311.9, 27.6/42.6/171.3, 26.3/37.4/128.8 and 328.1/394.1/429.7 mAh/g, respectively (Figure 6a). The results demonstrate that the RGO-B electrode exhibits the superior rate performance, with its advantage becoming particularly pronounced at high current densities. The charge-discharge

profiles and cyclic voltammetry (CV) spectra of RGO-B (Figure 6b,c) further reveal elongated sloping voltage plateaus in the electrode. The peaks observed at 1.1 V and 0.69 V in the first cycle correspond to SEI formation and Li^+ ion consumption via surface adsorption, respectively. The delithiation potentials consistently remain around 0.3 V with no offset after multiple cycles, indicating low polarization in the RGO-B electrode structure. This fully demonstrates the material's advantage over graphite by enabling Li^+ ion storage in higher potential regions, thereby effectively suppressing Li^+ plating. Cycling performance reveals that RGO-B delivers initial discharge/charge specific capacities of 781.0/609.7 mAh/g, which stabilize at 536.5/531.7 mAh/g after 50 cycles (Figures S19 and S20, Supporting Information). Figure 6d further demonstrates that the RGO-B electrode maintains a discharge specific capacity of 415.5 mAh/g after 800 cycles at 0.5 C, following the rate performance test. The charge transfer resistance values in the initial and 800th cycled states are 600 and 20 **Ω**, respectively, indicating significantly enhanced charge transfer capability during the cycling process (Figure 6e). Furthermore, the RGO-B electrode delivers an initial specific capacity of 60.5/74.9 mAh/g (ICE = 80.8%) at 13C. The capacity gradually increases to 169.8/170.2 mAh/g after 460 cycles (CE = 99.8%) and stabilizes at 115.5/115.9 mAh/g after 20,000 cycles (CE = 99.7%), with a capacity retention rate exceeding 100%. The low initial capacity is attributed to incomplete electrolyte infiltration, which hinders full access to the structural benefits. With progressive cycling, enhanced electrolyte wetting activates more ion-transport sites [39,42], leading to a capacity rise driven by deep electrochemical activation. The RGO-B//$LiFePO_4$ full cell maintains 153.0 mAh/g after 200 cycles, highlighting its potential for energy storage applications (Figure 6f,g).

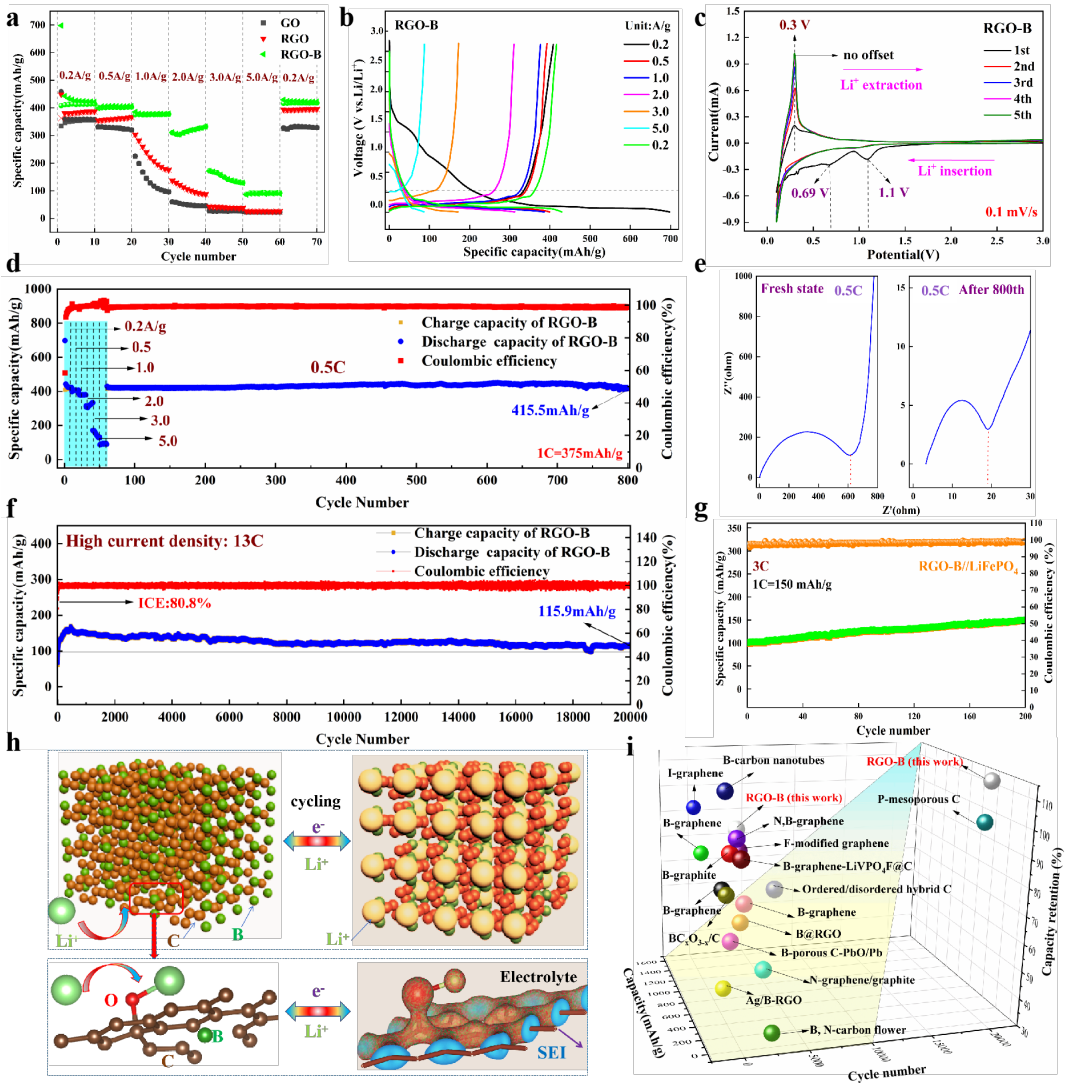

Figure 6. (**a**) Rate performance; (**b**) Charge-discharge profile; (**c**) CV spectra; (**d**) Combined rate and cycling performance at 0.5C; (**e**) EIS spectra; (**f**) Long-term cycling stability at ultra-high current density of 13C for 20,000 cycles; (**g**) Full-cell cycling performance; (**h**) Structural evolution during lithiation/delithiation processes; (**i**) Comparison for fast-charging LIBs of carbon-based anodes, which is obtained according to Table S6 (Supporting Information).

Electrochemical storage kinetic analysis of RGO-B electrode was characterized (Figure S21, Supporting Information). The pseudocapacitive contribution of the RGO-B electrode increased from 44.2 to 86.8% with the rise in scan rates from 0.1 to 1.0 mV/s. The pseudocapacitive contribution results reveal the dominant role of capacitive behavior and the fast Li^+ insertion/extraction characteristics of the capacitive storage mechanism. This enhanced performance can be primarily attributed to the deep penetration of B atoms into the RGO matrix via PRJH process, where the formed B–C/B-C-O bonds significantly regulate electronic structure, creating a surface with weaker negativity and higher work function, which eventually enhance the cycling stability under ultra-high rate. Combined with the aforementioned BET results, it is demonstrated that although RGO-B exhibits a slightly lower specific surface area, B doping significantly enlarges its pore size (from 13.6 nm to 21.2 nm) and introduces B-C/B-C-O active configurations. The lower specific surface area reduces the irreversible consumption of Li^+ ion during initial SEI formation, contributing to its high ICE, while the enlarged mesoporous structure lowers the resistance to Li^+ ion transport. Meanwhile, the additional active sites induced by B doping compensate for the potential capacity loss associated with the decreased surface area. The synergistic effect of these factors substantially enhances Li^+ ion transport kinetics, thereby enabling RGO-B to achieve optimal rate capability and cycling stability. A comparison of SEM images of the RGO-B electrode reveals that the layered structure remains largely intact even after 20,000 cycles, with no significant cracks observed across the entire electrode, which further corroborates the exceptional structural stability of RGO-B under ultra-long cycling at high rates (Figure 6h, Figure S22, Supporting Information). Figure 6i (Table S6, Figure S23, Supporting Information) demonstrates the superior high-rate charging capacity of RGO-B compared to diverse C-based materials in literature [43–51]. This highlights its exceptional characteristics such as green synthesis, short preparation time, and ultrahigh capacity retention, revealing its significant potential for widespread application in advanced battery systems.

4. Conclusions

In summary, this work presents a novel strategy for preparing B-doped reduced graphene oxide (RGO-B) without catalysts or solvents via a pulsed rapid joule heating (PRJH) method, which offer a more economically viable route for scalable doped graphene production. This technique simultaneously enables efficient O removal through thermal reduction and facilitates uniform and deep B incorporation via bulk-phase diffusion. DFT simulations reveal that the B-C bonds formed during PRJH process are highly favorable for both Li^+ ion and electron transport. Combined zeta potential and KPFM analyses confirm that deep B doping effectively modulates the electronic structure, yielding a less negatively charged surface with a higher work function-corroborating successful doping and directly accounting for the enhanced electrochemical behavior. The resulting RGO-B electrode delivers a charge specific capacity of 115.9 mAh/g after 20,000 cycles at an ultrahigh rate of 13 C, along with a capacity retention exceeding 100%, highlighting its exceptional promise for ultra-long-cycle energy storage applications.

Supplementary Materials

The additional data and information can be downloaded at: https://media.sciltp.com/articles/others/260618111374476/eChem-26030195-SI.pdf. Figure S1: The temperature-time scale of the RJH method and other heating treatments, Figure S2: (**a**) The circuit diagram of the dynamic pulsed rapid joule heating (PRJH) setup. (**b**) The optical photo of the PRJH vacuum chamber, Table S1: Experimental parameter design for PRJH process, Figure S3: Sequential optical images capturing the PRJH process from GO to RGO over four consecutive pulses in quartz tube with graphite paper, Figure S4: Sequential optical images capturing the PRJH process from RGO/B to RGO-B over ten consecutive pulses in quartz tube without graphite paper, Table S2: Mass yield for different PRJH processes, Figure S5: Unit cell configurations of different atomic structures, Table S3: Binding energy of all configurations, Table S4: Energy barriers of the Li migration process, Figure S6: Density of states (DOS) for different structural configurations: (**a**) RGO, (**b**) RGO-B1, (**c**) RGO-B2, (**d**) RGO-B3, Figure S7: Energy barrier for Li migration of Initial, Transition and Final states: (**a**) RGO, (**b**) RGO-B1, (**c**) RGO-B2, (**d**) RGO-B3, Table S5: Electron density difference distribution, Figure S8: I_D/I_G and I_{2D}/I_G ratios for GO, RGO and RGO-B, Figure S9: SEM images at different magnifications: (**a**) GO, (**b**) RGO, (**c**) RGO-B, Figure S10: TEM and SAED images at different magnifications for GO sample, Figure S11: TEM and SAED images at different magnifications for RGO sample, Figure S12: EDX elemental mapping and compositional analysis of local region ③ in RGO-B, Figure S13: Variation in the (002) lattice plane d-spacing, Figure S14: 2D and 3D color total maps and different element distributions for RGO-B (**a**) 3 cycles PRJH and (**b**) 10 cycles PRJH, Figure S15: Atom distribution via SIMS Analysis of RGO-B samples at different cycles PRJH for (**a**) B, (**b**) O and (**c**) C, Figure S16: Schematic illustration of B and O elemental migration during the PRJH process for (**a**) RGO/B and (**b**) RGO-B samples,

Figure S17: AFM Nano layer thickness variation for GO, RGO, RGO-B, Figure S18: Zeta potential of GO, RGO, RGO-B, Figure S19: Cycling performance of RGO-B at a current density of 0.1 A/g, Figure S20: Charge-discharge profiles of RGO-B at a current density of 0.1 A/g, Figure S21: Electrochemical storage kinetic analysis of RGO-B composite. (**a**) CV curves at different scan rates (0.1, 0.2, 0.4, 0.6, 0.8 and1.0 mV/s), (**b**) the fitting lines between log i and log v, (**c**) capacitive contribution in the CV curve (shaded region) at scan rate of 1.0 mV/s, and (**d**) the ratio of capacitive and diffusive contributions at different scan rates, Figure S22: SEM images of the RGO-B electrode: (**a**) Fresh state, (**b**) After 20,000 cycles, Table S6: Comparison for fast-charging LIBs of carbon-based anodes, Figure S23: Comparison for fast-charging LIBs of carbon-based anodes from views of (**a**) preparation time scale and (**b**) capacity retention after cycling. References [43–51] are cited in Supplementary Materials.

Author Contributions

K.W.: writing—original draft preparation, methodology, investigation, formal analysis, data curation, conceptualization; T.J.: data curation, visualization, investigation; X.Z.: data curation, visualization, investigation; Y.R.: data curation, visualization, investigation; F.H.: software, writing—reviewing and editing. Y.S.: formal analysis, resources; X.Z.: formal analysis, resources; Y.Z.: formal analysis, resources; Y.Z.: formal analysis, resources; J.L.: supervision, writing—reviewing and editing. H.W.: supervision, writing—reviewing and editing. All authors have read and agreed to the published version of the manuscript.

Funding

This work was supported by the Basic Research Programs of Shanxi Province in China (Grant No. 202403021221114, 202403021211075, 202303021212200 and 202303021211144). Shanxi Province Transformation Program of Scientific and Technological Achievements (No. 202304021301032), Shanxi Province Special Project for Scientific and Technological Cooperation and Exchange (No. 202404041101024).

Data Availability Statement

Data will be made available on request.

Conflicts of Interest

The authors declare no conflict of interest.

Use of AI and AI-Assisted Technologies

No AI tools were utilized for this paper.

References

1. Novoselov, K.S.; Geim, A.K.; Morozov, S.V.; et al. Electric Field Effect in Atomically Thin Carbon Films. *Science* **2004**, *306*, 666–669.
2. Geim, A.K.; Novoselov, K.S. The Rise of Graphene. *Nat. Mater.* **2007**, *6*, 183–191.
3. Papageorgiou, D.G.; Kinloch, I.A.; Young, R.J. Mechanical Properties of Graphene and Graphene-Based Nanocomposites. *Prog. Mater. Sci.* **2017**, *90*, 75–127.
4. Weiss, N.O.; Zhou, H.L.; Liao, L.; et al. Graphene: An Emerging Electronic Material. *Adv. Mater.* **2012**, *24*, 5782–5825.
5. Raccichini, R.; Varzi, A.; Passerini, S.; et al. The Role of Graphene for Electrochemical Energy Storage. *Nat. Mater.* **2015**, *14*, 271–279.
6. Jia, Y.R.; Zhang, J.; Kong, D.B.; et al. Practical Graphene Technologies for Electrochemical Energy Storage. *Adv. Funct. Mater.* **2022**, *32*, 2204272.
7. Chen, W.Y.; Ge, C.; Li, J.T.; et al. Heteroatom-Doped Flash Graphene. *ACS Nano* **2022**, *16*, 6646–6656.
8. Zhan, Y.F.; Zhang, B.D.; Cao, L.M.; et al. Iodine Doped Graphene as Anode Material for Lithium Ion Battery. *Carbon* **2015**, *94*, 1–8.
9. Wang, J.X.; Xia, Y.; Liu, Y.; et al. Mass Production of Large-Pore Phosphorus-Doped Mesoporous Carbon for Fast-Rechargeable Lithium-Ion Batteries. *Energy Storage Mater.* **2019**, *22*, 147–153.
10. Zhang, C.H.; Fu, L.; Liu, N.; et al. Synthesis of Nitrogen-Doped Graphene Using Embedded Carbon and Nitrogen Sources. *Adv. Mater.* **2011**, *23*, 1020–1024.
11. Scotland, P.; Eddy, L.; Chen, J.H.; et al. Heteroatom-Substituted Reflashed Graphene. *ACS Nano* **2025**, *19*, 11987–11998.
12. Wang, X.W.; Sun, G.Z.; Routh, P.; et al. Heteroatom-Doped Graphene Materials: Syntheses, Properties and Applications. *Chem. Soc. Rev.* **2014**, *43*, 7067–7098.

13. Wu, T.R.; Shen, H.L.; Sun, L.; et al. Nitrogen and Boron Doped Monolayer Graphene by Chemical Vapor Deposition Using Polystyrene, Urea and Boric Acid. *New J. Chem.* **2012**, *36*, 1385–1391.
14. Jung, S.M.; Lee, E.K.; Choi, M.; et al. Direct Solvothermal Synthesis of B/N-Doped Graphene. *Angew. Chem. Int. Ed.* **2014**, *126*, 2398–2401.
15. Wang, H.Q.; An, D.; Tian, P.Z.; et al. Incorporating Quantum-Sized Boron Dots into 3D Cross-Linked rGO Skeleton to Enable the Activity of Boron Anode for Favorable Lithium Storage. *Chem. Eng. J.* **2021**, *425*, 130659.
16. Jun, G.H.; Jin, S.H.; Lee, B.; et al. Enhanced Conduction and Charge-Selectivity by N-Doped Graphene Flakes in the Active Layer of Bulk-Heterojunction Organic Solar Cells. *Energy Environ. Sci.* **2013**, *6*, 3000.
17. Luan, Y.T.; Yin, J.L.; Zhu, K.; et al. Arc-Discharge Production of High-Quality Fluorine-Modified Graphene as Anode for Li-Ion Battery. *Chem. Eng. J.* **2020**, *392*, 123668.
18. Jeong, H.M.; Lee, J.W.; Shin, W.H.; et al. Nitrogen-Doped Graphene for High-Performance Ultracapacitors and the Importance of Nitrogen-Doped Sites at Basal Planes. *Nano Lett.* **2011**, *11*, 2472–2477.
19. Xiao, J.W.; Chen, Y.; Cai, C.H.; et al. Flash Joule Heating Synthesis of Nitrogen-Rich Defective g-C_3N_4 for Highly Efficient Photocatalytic Hydrogen Evolution. *Small* **2025**, *21*, 2503335.
20. Xiao, J.W.; Chen, Y.; Cheng, L.; et al. Flash Joule Heating: A Transformative Non-Equilibrium Strategy for Next-Generation Advanced Materials. *Small Methods* **2025**, *9*, e01678.
21. Luong, D.X.; Bets, K.V.; Algozeeb, W.A.; et al. Gram-Scale Bottom-Up Flash Graphene Synthesis. *Nature* **2020**, *577*, 647–651.
22. Eddy, L.; Xu, S.C.; Liu, C.H.; et al. Electric Field Effects in Flash Joule Heating Synthesis. *J. Am. Chem. Soc.* **2024**, *146*, 16010–16019.
23. Chen, W.Y.; Li, J.T.; Wang, Z.; et al. Ultrafast and Controllable Phase Evolution by Flash Joule Heating. *ACS Nano* **2021**, *15*, 11158–11167.
24. Stanford, M.G.; Bets, K.V.; Luong, D.X.; et al. Flash Graphene Morphologies. *ACS Nano* **2020**, *14*, 13691–13699.
25. Zhu, X.D.; Lin, L.T.; Pang, M.Y.; et al. Continuous and Low-Carbon Production of Biomass Flash Graphene. *Nat. Commun.* **2024**, *15*, 3218.
26. Deng, B.; Wang, Z.; Chen, W.Y.; et al. Phase Controlled Synthesis of Transition Metal Carbide Nanocrystals by Ultrafast Flash Joule Heating. *Nat. Commun.* **2022**, *13*, 262.
27. Eddy, L.; Luong, D.X.; Beckham, J.L.; et al. Automated Laboratory Kilogram-Scale Graphene Production from Coal. *Small Methods* **2024**, *8*, 2301144.
28. Wu, D.N.; Sheng, J.; Lu, H.G.; et al. Mass Production of Graphene Using High-Power Rapid Joule Heating Method. *Chem. Eng. J.* **2025**, *505*, 159725.
29. Yao, Y.G.; Huang, Z.N.; Xie, P.F.; et al. Carbothermal Shock Synthesis of High-Entropy-Alloy Nanoparticles. *Science* **2018**, *359*, 1489–1494.
30. Wang, C.W.; Ping, W.W.; Bai, Q.; et al. A General Method to Synthesize and Sinter Bulk Ceramics in Seconds. *Science* **2020**, *368*, 521–526.
31. Yao, Y.G.; Dong, Q.; Brozena, A.; et al. High-Entropy Nanoparticles: Synthesis-Structure-Property Relationships and Data-Driven Discovery. *Science* **2022**, *376*, 151.
32. Yao, Y.G.; Fu, K.K.; Zhu, S.Z.; et al. Carbon Welding by Ultrafast Joule Heating. *Nano Lett.* **2016**, *16*, 7282–7289.
33. Vashishth, S.; Vidyarthi, U.; Garg, A.; et al. Correlating the Mechanism, Kinetics, and SEI Formation of a Boron-Doped Graphene Anode for High-Performance Alkali Ion Batteries. *J. Mater. Chem. A* **2025**, *13*, 25749–25761.
34. Wan, J.; Liu, L.; Wu, Y.; et al. Exploring the Polarization Photocatalysis of $ZnIn_2S_4$ Material Toward Hydrogen Evolution by Integrating Cascade Electric Fields with Hole Transfer Vehicle. *Adv. Funct. Mater.* **2022**, *32*, 2203252.
35. Adekoya, D.; Qian, S.S.; Gu, X.X.; et al. DFT-Guided Design and Fabrication of Carbon-Nitride-Based Materials for Energy Storage Devices: A Review. *Nano-Micro Lett.* **2021**, *13*, 13.
36. AlJaber, G.; AlShammari, B.; AlOtaibi, B. From Theory to Experiment: Reviewing the Role of Graphene in Li-Ion Batteries Through Density Functional Theory. *Nanomaterials* **2025**, *15*, 992.
37. Gavali, D.S.; Kawazoe, Y.; Thapa, R. First-Principles Identification of Interface Effect on Li Storage Capacity of C_3N/Graphene Multilayer Heterostructure. *J. Colloid Interface Sci.* **2022**, *610*, 80–88.
38. Wang, K.; Chen, J.C.; Hou, F.X.; et al. In Situ Growth-Optimized Synthesize of Al-MOF@RGO Anode Materials with Long-Life Capacity-Enhanced Lithium-Ion Storage. *Chem. Eng. J.* **2023**, *455*, 140561.
39. Wu, Z.S.; Ren, W.C.; Xu, L.; et al. Doped Graphene Sheets as Anode Materials with Superhigh Rate and Large Capacity for Lithium Ion Batteries. *ACS Nano* **2011**, *5*, 5463–5471.
40. Wang, H.Q.; Li, Y.; Wang, Y.Z.; et al. Highly Microporous Graphite-Like BC_xO_{3-x}/C Nanospheres for Anode Materials of Lithium-Ion Batteries. *J. Mater. Chem. A* **2017**, *5*, 2835–2843.
41. Wang, K.; Zhong, X.B.; Song, Y.X.; et al. Regeneration of Photovoltaic Industry Silicon Waste Toward High-Performance Lithium-Ion Battery Anode. *Rare Met.* **2024**, *43*, 4948–4960.

42. Lee, J.; Moon, J.; Han, S.A.; et al. Everlasting Living and Breathing Gyroid 3D Network in Si@SiO_x/C Nanoarchitecture for Lithium Ion Battery. *ACS Nano* **2019**, *13*, 9607–9619.
43. Sahoo, M.; Sreena, K.P.; Vinayan, B.P.; et al. Green Synthesis of Boron Doped Graphene and its Application as High Performance Anode Material in Li Ion Battery. *Mater. Res. Bull.* **2015**, *61*, 383–390.
44. Park, M.S.; Lee, J.; Lee, J.W.; et al. Tuning the Surface Chemistry of Natural Graphite Anode by H_3PO_4 and H_3BO_4 Treatments for Improving Electrochemical and Thermal Properties. *Carbon* **2013**, *62*, 278–287.
45. Liu, X.X.; Liu, E.J.; Chao, D.L.; et al. Large Size Nitrogen-Doped Graphene-Coated Graphite for High Performance Lithium-Ion Battery Anode. *RSC Adv.* **2016**, *6*, 104010.
46. Wang, H.Q.; Li, Y.; Wang, Y.Z.; et al. Three-Dimensional B-Doped Porous Carbon Framework Anchored with Ultrasmall PbO/Pb Nanocrystals for Lithium Storage. *Ceram. Int.* **2017**, *43*, 12442–12451.
47. Bindumadhavan, K.; Chang, P.Y.; Doong, R.A. Silver Nanoparticles Embedded Boron-Doped Reduced Graphene Oxide as Anode Material for High Performance Lithium Ion Battery. *Electrochim. Acta* **2017**, *243*, 282–290.
48. Wang, L.; Guo, W.L.; Lu, P.Y.; et al. A Flexible and Boron-Doped Carbon Nanotube Film for High-Performance Li Storage. *Front. Chem.* **2019**, *7*, 832.
49. Yang, Y.A.; Chen, C.; Sun, H. $LiVPO_4F$@C Particles Anchored on Boron-Doped Graphene Sheets with Outstanding Li^+ Storage Performance for High-Voltage Li-Ion Battery. *Solid State Ion.* **2019**, *331*, 6–11.
50. Zhao, Y.X.; Li, Y.; Zheng, N.; et al. Boron and Nitrogen Double-Doped Carbon Flower Prepared by In-Situ Copolymerization as Anode Materials for Lithium-Ion Batteries. *J. Appl. Polym. Sci.* **2023**, *140*, e53544.
51. Huang, P.F.; Li, Z.K.; Chen, L.; et al. Ultrafast Dual-Shock Chemistry Synthesis of Ordered/Disordered Hybrid Carbon Anodes: High-Rate Performance of Li-Ion Batteries. *ACS Nano* **2024**, *18*, 18344−18354.